INVESTIGATING THE POTENTIAL OF THE OPERATIONAL LAND IMAGER (OLI) FOR MONITORING CASE II WATERS USING A LOOK-UP-TABLE APPROACH

Nima Pahlevan
John R. Schott
Center for Imaging Science
Rochester Institute of Technology
54 Lomb Memorial Drive
Rochester, NY 14623
nxp5492@cis.rit.edu
schott@cis.rit.edu

ABSTRACT

Monitoring ocean and coastal waters, recognized as case II waters, using the existing Landsat technology is somewhat restricted because of its low Signal-to-Noise ratio (SNR) as well as its relatively poor radiometric resolution. The new generation of Landsat, Landsat Data Continuity Mission (LDCM) carrying Operational Land Imager (OLI), has enhanced features allowing for better characterization of water constituents in either coastal or oceanic waters with respect to Landsat 7 (L7). This paper applies a physics-based model to examine the potential of OLI with respect to L7 in monitoring coastal waters. The OLI imagery was modeled via spectrally resampling Hyperion dataset followed by removing atmospheric effects. An in-water radiative transfer model, i.e. Hydrolight, was applied to generate a Look-Up-Table (LUT) of simulated water-leaving reflectances for various combinations of water constituents. Absorption properties of in-water components were measured in turbid waters, whereas scattering coefficients were estimated by optimizing modeled surface reflectances against *insitu* measured surface reflectances. The water constituent retrieval was conducted on a pixel-by-pixel basis by searching the LUT for a simulated reflectance curve which minimizes a cost function against the corresponding OLI- and L7-derived surface reflectance. The chlorophyll concentration map derived from the simulated OLI imagery, on average, showed a good agreement with MODIS-derived products in turbid and clear water. The concentration of total suspended solids obtained in the proximity of the river mouth also indicated a strong correlation with *insitu*-measured concentrations. This study verified that OLI outperforms Landsat 7 in mapping water quality parameters while Landsat 7 tends to overestimate the water constituent concentrations.

Keywords: OLI, Landsat 7, water constituents, Niagara River plume, coastal/inland waters

INTRODUCTION

The main objective of this paper is to investigate the capability of the new generation of Landsat (LDCM) relative to Landsat 7 (L7) in mapping/monitoring water constituents in coastal waters. The water constituent retrieval is validated against MODIS-derived products as well as *insitu* measurements.

Remote sensing has long been recognized to serve the science community with invaluable data on the distribution of critical in-water components including chlorophyll (CHL) and Colored Dissolved Organic Matter (CDOM) which drive ecological and chemical processes in open waters (Jensen, 2006). However, retrieving water quality parameters in coastal/inland waters, known as case II waters, is not an easy task due to runoffs and discharges from rivers/streams, which add to the complexity of the water constituent retrieval process. Inflows from land-based waters introduce different organic/inorganic particles, known as Total Suspended Solids (TSS). Not only do particles alter the physical and biological processes in coastal waters, but also they contribute to increase the magnitude of water-leaving optical signatures because of their high-scattering nature (Mobley, 1994; Binding *et al.*, 2005; Bowers *et al.*, 2009). As opposed to particles, CHL and CDOM are absorbing components with CDOM absorbing in short wavelengths (350-440 *nm)* and CHL representing two absorption peaks in the blue and red regions of the spectrum at 440 *nm* and 670 *nm* respectively. In addition to the optical signature of pure water, the signal emanating from case II waters is also influenced by concentrations of CHL, TSS, and dissolved organic matter along with their Inherent optical Properties (IOP). Water constituent retrieval in such environments using optical remote sensing requires several spectral channels in the Visible-Near-Infrared (VNIR) to capture subtle

differences in the upwelling optical field. Hence, hyperspectral remote sensing, equipped with many narrow spectral bands, provides a great means for water constituent retrieval in case II waters (Hakvoort *et al.*, 2002; Thiemann and Kaufmann, 2002). However, until the successful launch of Hyperion, hyperspectral imaging (HSI) was restricted only to airborne missions, which significantly adds to the necessary costs for regular monitoring of extensive areas. Since 2001, Hyperion, equipped with approximately 70 bands in the VNIR, has enabled scientists to study water bodies of different types on a regular basis (~ 1-3 days) with a spatial resolution on a similar order as L7. Despite having numerous spectral channels to investigate water features, Hyperion suffers from low SNR due to its design specification and the limited number of photons reaching the imaging device within each spectral band. The low signal level arising from the water in these narrow bands is largely affected by the atmospheric effects, especially in the short blue bands, making atmospheric correction a vital task in the HSI image processing chain (Sanders *et al.*, 2001). Thus, in any water constituent retrieval task atmospheric effects must be properly modeled and removed using an appropriate algorithm (Gordon, 1978).

The Moderate Resolution Imaging Spectrometer (MODIS) and the Sea-viewing Wide Field-of-view Scanner (SeaWiFS) are the two imaging systems developed and designed, in late 1999, for regular monitoring of global/regional waters (Gordon, 1990). In particular, MODIS along with appropriate experimental techniques and modeling efforts has successfully been able to deliver vital image products for evaluating global primary production, dissolved oxygen carbon budget, sea surface temperature (SST), and many others. Although the two sensors have been spectrally and radiometrically configured for water studies, with a ground-sample distance (GSD) greater than 500 *m*, their applicability is limited to large bodies of water where no mixed pixels exist. This is especially an issue when the remote sensing task or the scientific requirements demand detailed spatial scale (<100 *m*), e.g. small bays, lakes, and river discharges. Satellite remote sensing utilizing multispectral imaging systems that are able to provide spatial resolutions that meet the science requirements are reasonable choice for case II studies. The detailed spatial demand makes the use of commercial satellites, such as IKONOS, QuickBird, and the recently launched WorldView-2, intriguing alternates. However, for monitoring purposes, the procurement of such imagery puts a significant cost burden on a project and has to be properly justified.

Landsat, designed primarily for monitoring land targets, appears to offer a reasonable spatial detail over in costal waters; however, its limited radiometric resolution, i.e., 8-bit quantization level, makes it difficult to discern inter-pixel spatial variability. It also suffers from a low Signal-to-Noise Ratio SNR over dark targets such as water bodies. The new generation of Landsat, which is planned to be launched in 2012, carries two imaging instruments, namely Operational Land Imager (OLI) and the Thermal Infrared Scanner (TIRS), to monitor earth phenomenology through both reflective and thermal atmospheric windows. OLI is a pushbroom system with linear detector arrays oriented across track with GSD of 30 *m*. Its pushbroom design allows for longer integration time resulting in higher SNR. Moreover, OLI acquires imagery in eight spectral bands with 12-bit radiometric resolution. Theoretically, the addition of a coastal/aerosol (CA) band, centered at 443 *nm*, along with its superior radiometric fidelity should lead to more accurate water constituent maps relative to those produced from Landsat 7 (Gerace, 2010).

This paper aims at retrieving water constituents, including concentrations of TSS and CHL as well as CDOM absorption, using simulated OLI imagery derived from the Hyperion data of the Niagara River plume discharging into Lake Ontario. The OLI-derived constituent distribution maps are then compared to those obtained from L7 to determine the improvement levels and the discrepancies between the two instruments in such tasks. The outputs are validated against MODIS-derived CHL products and *insitu* measurements.

METHODOLOGY

As briefly described in the previous section, the primary objective of any water constituent retrieval process using remote sensing is to estimate the concentration/optical properties of optically active components of water, i.e., concentrations of CHL and TSS as well as CDOM absorption. In this study, the constituent retrieval task is attempted for the Niagara River plume and its surrounding waters in the western basin of Lake Ontario. The study site and the dataset is described in the following section. This is followed by data pre-processing and atmospheric compensation to derive water-leaving reflectance (ρ). The final section elaborates on the water constituent retrieval process, based upon Hydrolight simulations.

Study Area and Dataset

For the purpose of this research, the Niagara River plume discharging into Lake Ontario was studied. The 57 *km* Niagara River, which runs northward from Lake Erie, is the major source of inflow into Lake Ontario.

Table 1. Imaging geometry conditions

	L7	EO1
Sun elevation*	34.5	32.9
Sun azimuth	160.4	153.9
Off-nadir	6.1	20.1
Sensor azimuth	278.2	98.2

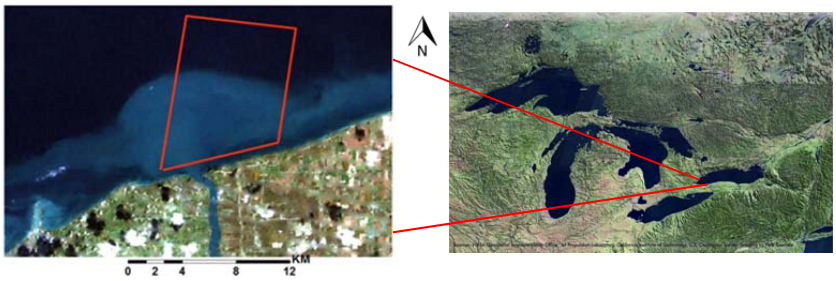

Figure 1. Study area covering the Niagara River plume (left) discharging into the western basin of Lake Ontario. The red box (~ $100\,km^2$) indicates the ROI.

The river is the drainage outlet for the four upper Great Lakes (Figure 1) having an aggregate basin area of $670{,}000\,km^2$. In addition, as water is carried away from Lake Erie, all of the nutrient loads and nuisance algae, from both the US and Canadian sides, are transferred into Lake Ontario through the river. The Niagara River discharge is estimated, on average, to exceed $5500\,m^3/s$, which represents 80% of the total water flow into the Lake (Hayashida *et al.*, 1999). Figure 1 shows the geographic location of Lake Ontario with the Niagara River entering its western basin. The region of interest (ROI) encompasses turbid, river plume waters, from Lake Erie, as well as clear waters of Lake Ontario. Therefore, the water constituent retrieval is conducted for both turbid and relatively clear waters in this study.

L7 imagery, row-path 30-18, acquired on October 19th 2010 at 11:56AM EST, was used for this study. The L7's scanning mirror imaged the western basin of Lake Ontario while pointing slightly westward. Nearly simultaneously with the L7 overpass, EO1, tasked over the study area at $(43.33^{\circ}\text{N}\ ,\ 79^{\circ}\text{W})$, collected a pair of images with its dual instruments, namely Hyperion and the Advanced Land Imager (ALI). The imaging geometry parameters for EO1 and L7 are listed in Table 1. It was assumed that any effects caused by the differences in viewing geometry and the Bidirectional Reflectance Distribution Functions (BRDF) were minimal. This is a valid assumption as uncertainties corresponding to atmosphere and IOP estimation would dominate the error budget in the constituent retrieval errors. In spite of operating with similar design and spectral configurations relative to OLI, ALI data was discarded in this study. This is primarily related to its calibration issues, i.e., non-uniform responses between its four sensor-chip-assemblies (SCAs) as well as the discrepancies in the Relative Spectral Responses (RSR) of the two sensors. The latter issue would bias our study of OLI in the constituent retrieval task. Figure 2 illustrates the RSR profiles of L7, OLI and ALI (Barsi, 2011). The differences in the RSRs are most noticeable for the bands where the signal reaching the sensors are the highest. Hence, the disparity between the OLI and the ALI's RSR of CA band introduces some bias when examining OLI. It should also be noted that L7 does not have the new CA band designed for OLI.

Data Pre-processing

After 2003, the scan-line correctors (SLC) of L7 failed to function, forming gaps, in some of the image area. For visualization purposes, the missing pixels were filled via a spatial interpolation technique; however, the constituent retrieval maps were analyzed with the gaps masked out. Although the L1G standard L7 product, obtained from USGS web service, was used for this study, the imagery exhibited significant miss-registration errors. The L7 imagery, therefore, was locally co-registered to Hyperion data with a 2nd order polynomial function (RMSE < 0.3 pixel). The coastline and Niagara River's features of the corrected L7 data were further validated with a bathymetry map made available by NOAA's National Geophysical Data Center to ensure an accurate co-registration. The Digital Counts (DCs) of each individual image band were converted to Top-of-Atmosphere (TOA) radiance quantities $[W/m^2 sr\ \mu m]$ by applying the band-specific gain and offset coefficients available in the metadata. Hyperion data was first de-striped using the statistical ratio technique for pushbroom systems (Schowengerdt, 2007) followed by conversion to TOA radiance values $[W/m^2 sr\ \mu m]$.The HSI data were then

* All of the units are in degrees.

spectrally resampled to OLI's RSR functions to simulate what OLI "sees" through its eight spectral bands. After more than 10 years of operation, the radiometric fidelity of Hyperion, particularly in the short blue bands, is somewhat degraded. Calibration issues associated with other regions of the spectrum were also revealed when compared to the TOA radiance curves derived from MODTRAN simulations as well as the Aqua-MODIS data.

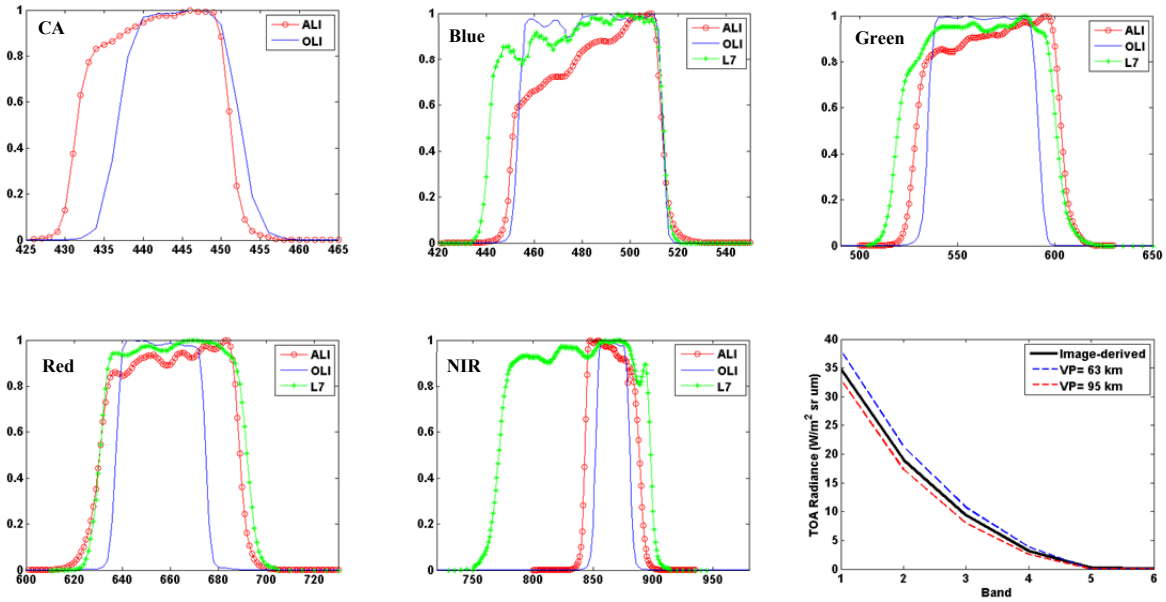

Figure 2. The band-specific, normalized RSRs of L7, OLI, and ALI shown for different portions of the spectrum [*nm*]. The differences are discernable in all of the bands, in particular in the NIR band. Also, the L7-derived TOA radiance is illustrated against those derived from the simulations.

In order to compensate for the miss-calibration, the simulated OLI images of TOA radiance were regressed against Aqua-MODIS L1B-500*km* calibrated products for multiple dates over dark uniform waters. The Short-Wave-InfraRed (SWIR) responses of the multiple pairs of images were statistically compared to ensure similar atmospheric conditions. The simulated VNIR OLI imagery was calibrated via applying offset coefficients, additive/subtractive, obtained in the regression process.

Atmospheric Removal

When imaging low reflective targets, such as water, the total signal reaching the sensor is substantially contaminated by the molecular/aerosol scattering in the atmospheric target-sensor path. There has been a tremendous amount of research in developing algorithms/methods for atmospheric compensation over waters. The majority of the algorithms rely upon the zero-reflectance assumption in the long, reflective solar bands ($\lambda > 800\ nm$) where photons reaching the imaging instrument emanate solely from the atmospheric path. These methods, however, require reasonably high SNR (>10) for such bands, which is not available for L7. Other methods, such as spectral matching and the use of water vapor absorption bands, apply to HSI imagery (Sanders *et al.*, 2001).

In this paper, a pseudo-spectral matching, implemented over the first four bands of L7, has been applied. This method utilizes MODTRAN to simulate different atmospheric conditions for various combinations of aerosol types (AT) and visibility parameters (VP) (Berk *et al.*, 1989). Knowing the upper-atmosphere radiosonde data, the surface reflectance associated with dark waters, and the acquisition geometry, MODTRAN is able to model total TOA radiance of multiple pairs of AT and VP. The modeling result is a look-up-table (LUT), or a stack of TOA radiance curves, of various atmospheric conditions, out of which one represents the minimum disparity relative to a corresponding image-derived curve. The TOA curve obtained from the dark waters is obtained by taking an average over the darkest pixels in the proximity of the study area. By minimizing the Mahalanobis distance metric the best fit resulted from rural aerosol type of VP=84 *km* exhibited the closest match with the image-based curve. Figure 2 shows the L7-derived curve overlaid on the two modeled curves representing extreme atmospheric conditions, i.e. VP=63 *km* and VP=95 *km*. For consistency, OLI data was atmospherically corrected using identical atmospheric conditions. This is a valid assumption as the images are acquired only 20 minutes apart. With the knowledge of

atmospheric condition, the remote sensing governing equation (Schott, 2007) was then solved for water-leaving reflectance, $\rho(\lambda)$:

$$L(\lambda) = [E_{s\lambda} \cos(\sigma_s)\tau_1(\lambda)\rho(\lambda)/\pi + L_{d\lambda}\rho(\lambda)]\tau_2(\lambda) + L_{u\lambda} + r_f \ \tau_2(\lambda)L_{d\lambda} \quad (1)$$

where $L(\lambda)$ denotes the image-derived TOA radiance $[W/m^2 sr\ \mu m]$, $E_{s\lambda}$ represents the exo-atmospheric solar irradiance $[W/m^2\ mu]$, σ_s stands for solar zenith angle, τ_1 is the solar-earth path transmission, $\rho(\lambda)$ is the unitless water-leaving reflectance, $L_{d\lambda}$ is the downwelled sky radiance $[W/m^2 sr\ \mu m]$, τ_2 is the sensor-earth path transmission, and $L_{u\lambda}$ indicates path radiance $[W/m^2 sr\ \mu m]$ which is the cumulative effects of molecular and aerosol scattering. The last term is an additional term that takes into account sky glint resulting from diffuse downwelled sky light reflected off the water surface. For this study, the Fresnel reflection coefficient is assumed constant for all of the spectral bands ($r_f = 0.02$). It is also assumed that water has properties of a Lambertian surface and has no angular dependency over the imaging geometry condition. The surface reflectance (SR) spectra were then resampled to OLI RSR functions to gain the multispectral SR curves.

Water Constituent Retrieval

In order to quantify water constituents on a pixel-by-pixel basis, an in-water radiative transfer model, called Hydrolight, was utilized. Hydrolight is a time-independent, plane-parallel radiative transfer model, which predicts the radiance distribution of a light field within and out of a water body (Mobley, 2008).

Hydrolight initialization. The model is provided with the wavelength-dependent IOPs including scattering and absorption coefficients of CHL and TSS as well as CDOM absorption. The standard Pop-Fry's absorption and scattering coefficients of pure water were used for this study. Based on retrospective experimental attempts, the 2% Fournier-Forand backscattering phase functions for CHL and TSS were adopted for this study where moderately turbid waters are investigated.

Field/IOP measurement. A field campaign was conducted in the Niagara River on the same day the L7 and Hyperion acquired the images. During the campaign, spectrometry measurements were collected at two different locations along the river on the USA side. Along with these measurements, multiple water samples from four different locations in the river were collected and transferred to the laboratory for further analysis. The absorption coefficients associated with CHL, TSS, and CDOM were empirically derived through the quantitative filter technique (QFT) (Binding *et al.*, 2008). In doing so, 25*mm* Whatman filters were applied for water sample filtration followed by absorbance measurements using a UV-2100 Shimudzo dual-beam spectrophotometer, configured on the slow scanning mode with 5nm slit width. The CDOM absorption spectrum was also obtained using 10 *cm* standard cuvette with the same instrument. While TSS concentration was measured gravimetrically, CHL concentration measurements were performed using the standard spectrometry method. Although the absorption spectra for all of the constituents were measured by the laboratory analysis, the scattering coefficients were estimated through a curve-fitting method in which different modeled reflectance spectra were compared to the averaged *insitu* measured reflectance spectra. Various TSS/CHL scattering coefficients were attempted to generate several reflectance spectra, out of which one exhibited the best agreement with the corresponding spectrum measured on site. It should be noted that, for these simulations, other model inputs were held unchanged, allowing for deriving physically realistic scattering coefficients.

LUT generation. The procedure followed here is based upon the principles described in (Raqueno, 2003) . Raqueno, 2003, tested this approach on the HSI imagery, i.e. Airborne Visible/Infrared Imaging Spectrometer (AVIRIS) dataset, in the Rochester Embayment. In this method, a LUT of various combinations of water constituents is populated in a 3D space. Associated with each triplet of constituents, a modeled SR is generated using a single simulation. Many simulations are required to find the modeled SR for all of the combinations of water constituents. Here, a very finely sampled LUT was designed to minimize any possible errors due to optimization techniques. The increments for CHL and TSS concentrations were chosen to be 0.1 units of concentrations whereas CDOM absorption was scaled by multiplication factors incremented by 0.2 [*unitless*]. Throughout this paper, the TSS and CHL concentrations are expressed in $[gm^{-3}]$ and $[ugl^{-1}]$, respectively, unless otherwise mentioned. The CDOM absorption at 440 *nm*, $a_{CDOM}(440) = 0.14\ m^{-1}$, measured in turbid river waters, was treated as a basis and scaled within the range of 0.1 to 5.0 to capture a wide spectrum of CDOM absorption spectra. The best combination of water constituents for an image pixel is the one that gives rise to the minimum disparity between the modeled SR

and the one derived for the associated L7 and OLI pixel. The cost functions defined to select for the best fit are Root-Mean-Squared Error (RMSE) and percent difference error (PD). In addition to SR values for individual bands, the band ratios of blue-green (B-G) for L7 and OLI and CA-blue (CA-B) only for OLI were incorporated in the search process to enhance the separaibility and uniqueness of the matching spectrum. Prior to implementing the LUT search, bad pixels, the ones assigned with negative values in any bands due to quantization errors or low SNR, were discarded in the two images. While recognizing that incorporating the Near InfraRed (NIR) band can improve the retrieval process for case II waters, it was decided to ignore this band owing to the significant increase in the simulation times as well as low SNR of the simulated OLI NIR band.

Image segmentation and smoothing. Although measured/estimated in the Niagara River, the IOPs may not represent the optical properties of relatively clear waters containing low TSS levels. Moreover, in clear, case I waters, the IOP model has only two components, i.e., CHL and CDOM absorption. Thus, a different absorption spectrum, which appears to represent an averaged CHL absorption spectrum for Lake Ontario, was selected for areas with substantially low sediment concentration ($< 0.8\, gm^{-3}$). In doing so, the images were classified in a supervised fashion to divide the area into two regions attributed with two different CHL absorption spectrum. The two regions are distinguishable in Figure 3.

The SNR of the simulated OLI data is relatively low with respect to the design specifications of the OLI onboard LDCM. In fact the simulated OLI imagery has SNRs approximately one-third of the specifications. In order to simulate a more realistic capability of OLI for water quality studies, the image-derived SNR was improved three times by taking the average of nine neighboring pixels surrounding each individual pixel. The retrieval process was then attempted on the smoothed L7 and OLI imagery.

Along with water constituent maps, pixel-by-pixel error maps were also generated to understand the goodness of fit of each individual pixel's multispectral data points to that of the matched modeled curve. The error maps (*EMAPs)* are calculated as follow (Eq. 2):

$$EMAP_{i,j} = \left| \left(Obs_{i,j} - Mod_{i,j} \right) \left(Obs_{i,j} + Mod_{i,j} \right)^{-1} \right| \quad (2)$$

where *i* and *j* are pixel locations, and *Obs* and *Mod* denote the image- and the model-derived values, respectively.

RESULTS AND DISSCUSSIONS

As noted, the final products of this study include water constituent maps illustrating surface distribution of the corresponding constituents derived from L7 and the simulated OLI imagery. In order to be able to make a reasonable comparison between the two products, it is necessary to evaluate the uncertainties in the processing chain which led to the SR products from which the constituent maps were derived. Although the primary uncertainty is related to the fidelity of the atmospheric compensation, the calibration issues associated with the instruments, in particular with the simulated OLI, may introduce inconsistencies in such a comparative study. Moreover, such issues manifest themselves in the SR products created from the pre-processing procedure. Therefore, statistical investigation of the SR maps reveals any inconsistencies in the processing chain and provides better insights into the accuracy assessment of the final products.

Surface Reflectance Analysis

The SR products were generated by removing atmospheric effects using the MODTRAN code. Prior to the atmospheric compensation, however, the simulated OLI TOA radiance imagery was adjusted relative to that of MODIS data to ensure its compatibility with MODTRAN-derived simulations as well as with the L7 data. It should be mentioned that the assumption is that L7 bands are well calibrated and there is no need for further corrections.
Table 2 contains the relevant statistics allowing for understanding the differences between the OLI and L7 products. The SRs obtained from L7/OLI were also analyzed against MODIS-derived products and Hydrolight simulations. The metrics are calculated over several pixels selected throughout the plume area when making image-to-image comparison. However, the simulated quantities, derived from Hydrolight, were analyzed against OLI- and L7-derived averaged pixels selected from the vicinity of the river mouth where IOPs and concentrations were measured. The very close pixels (< 30) to the shoreline were avoided to prevent adjacency effects. It turns out that the largest differences between OLI and L7 appear in the red band where more than a 14% difference exists between the two products. A similar trend is observed when comparing L7 red channel products with those obtained from MODIS and simulations. This trend is most likely caused by stray light in the L7 instrument which produces unwanted

signals that boost which boost the signal reaching the aperture. This disparity in the red band may contribute to some inconsistencies in the constituent retrieval process. A similar comparison was also made in the clear waters, not listed in the table for brevity. In clear waters, L7 tends to overestimate the signal in the red band more than 35%, on average, when compared to the simulations and MODIS/OLI SR products. Nevertheless, the signal differences in the two other bands lie in a reasonable range, i.e., (< 10%), even though the variability in reflectance is relatively large, i.e., standard deviations of 40% and 18% in the blue and green bands, respectively.

Table 2. The relative errors, expressed in percent difference and RMSE, between the SRs throughout the turbid waters

	CA		Blue		Green		Red	
	OLI	L7	OLI	L7	OLI	L7	OLI	L7
OLI		NA		1.5% 0.07		1.2% 0.05		14.5% 0.24
MODIS	3.9%*	NA	4.3% 0.12	5.5% 0.18	3.2% 0.09	4.1% 0.15	0.5% 0	16.8% 0.28
Simulated	0.5%	NA	0.8%	2.2%	0.7%	0.4%	4.8%	10.1%

The higher overall errors in clear waters suggest that errors should be treated as bias and support our speculation on the stray light as the source. Note that this type of calibration artifact is negligible when sensing medium- to high-level reflective targets ($\rho > 10\%$). The disparities identified between the OLI and L7 SR products helps in understanding the differences between the water constituent maps.

Water Constituent Maps

According to the characteristics of the two imaging systems, a handful of pixels with negative SR values in any individual band were identified. The retrieval algorithm was adapted to discard such "bad" pixels. In doing so, 4% and less than 0.5% of the total number of pixels were ignored in L7 and OLI data, respectively. Figure 3 illustrates the constituent maps derived from L7 and OLI products.

TSS maps. In general, the two TSS maps generated using the model-based retrieval algorithm exhibit a relatively good correlation (r >0.4). However, the TSS map derived from L7 (TSS-L7) were assigned with higher values in the plume area. As sensitivity studies have shown in previous studies, there is a strong, positive correlation between the TSS concentration and L7 red channel. It can be inferred that the calibration issue associated with this band largely leads to the overestimation of TSS concentration. The $0.21\, gm^{-3}$, on average, overestimation of TSS-L7 concentration with respect to that of OLI (TSS-OLI) amounts to 10.5% difference in concentration over the plume area. The similar trend was identified in the proximity of the river mouth where *insitu* measurements of TSS concentration were available. TSS-OLI showed 6.1% error relative to the field measurements whereas 14.1% error was calculated for TSS-L7. Although TSS-L7 shows considerable variability in clear waters, the average TSS concentrations estimated by L7 closely resemble that obtained from OLI. Appendix A shows the statistics associated with water TSS/CHL concentration maps.

CHL maps. When comparing CHL products, it is clear that OLI outperforms L7 as it produces a reasonable CHL concentration map with respect to the MODIS-derived (CHL-MODIS) concentrations with, on average, errors less than 10%. L7 tends to overestimate CHL throughout both turbid and clear waters. As shown in Appendix A, CHL-OLI over the plume area represents the highest correlation (negative) with the CA band whereas the correlation with the green band is insignificant. On the other hand, CHL-L7 shows the highest, positive correlation with the red band, i.e., 0.44, over the plume area. There is no significant correlation between CHL-L7 and green band. In clear waters, CHL-L7 has a relatively high correlation with the blue band while the CHL-OLI exhibits the highest correlation with the CA band, i.e., -0.66.

It should also be noted that the constituent retrieval method was constrained to ignore the out-of-bound CHL concentrations (> $3.6\, ugl^{-1}$) or the pixels for which a unique minimum error were not achieved, i.e., more than one combination of constituents resulted in an identical minimum error. In doing so, the algorithm masked out more than 35% of the total number of pixels when retrieving CHL-L7. That being said, less than 1% of OLI data were

* The CA band data was obtained from Aqua-MODIS since the short blue band of Terra-MODIS is degraded.

discarded which implies its higher SNR and its superior radiometric fidelity, i.e., 12-bit quantization rate. The predicted CHL-L7 concentrations, lying in the range of 0-3.5 ugl^{-1}, represent approximately, on average, 15% higher concentrations, after removal of masked pixels, over the plume and clear waters relative to CHL-MODIS. However, if out-of-bound values (> 3.6 ugl^{-1}) are ignored CHL-L7 underestimates the concentrations up to 20%. The CHL-OLI products when downsampled to MODIS's spatial resolution showed a good agreement with CHL-MODIS products, i.e., < 8% error, over the plume and clear waters (Appendix A). The results indicate improvements in determining CHL concentration via the addition of the CA band when compared to the CHL-MODIS.

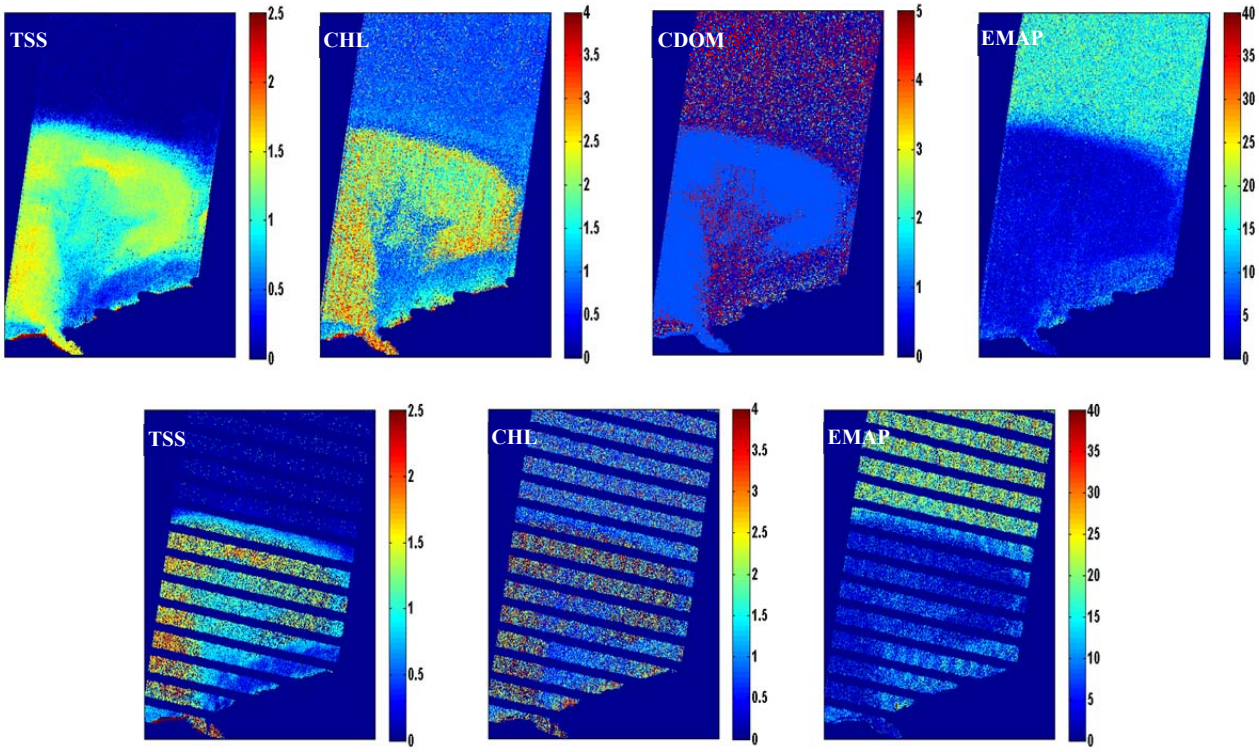

Figure 3. Water constituent maps derived from simulated OLI (upper row) and L7 surface reflectance products. The maps from left to right denote TSS, CHL, CDOM, and error maps. The error maps, expressed in percent error, denote higher errors in the very low-reflectance clear waters. The L7-derived CDOM is not shown as L7 is not capable of retrieving the CDOM variations. The SLC-off effects on L7 are shown to avoid interpolation effects.

The fact that CHL-OLI is correlated with the CA band explains the high local variability of (Figure 3) as Hyperion's short blue bands have a low SNR resulting in noise induced variability.

CDOM index maps. As expected, L7 is not useful for mapping CDOM absorption due to its broad blue band centered at 475 *nm*. However, OLI, equipped with the CA band should exhibit some sensitivity to variations in CDOM absorption at 440 *nm*. This has been proven in this study where CDOM absorption values establish a good correlation with CA and CA-B ratio bands. However, the CA band of the simulated OLI data are derived by aggregating four short blue bands (bands 8-11) of Hyperion. These bands are attributed with low SNR, i.e., approximately 75 over dark waters, which exacerbates our estimation of CDOM absorption from the OLI dataset. The mean value of 1.1 for the CDOM scaling factor, which is equivalent to $a_{CDOM}(440) \approx 0.15\, m^{-1}$, found in the surroundings of the plume appears to resemble average Lake Ontario's CDOM absorption index. Retrieving CDOM absorption in turbid/clear waters with OLI's CA band is somewhat restricted to the TSS/CHL concentration. High absorption of suspended particles and chlorophyll in the short blue bands along with their high concentrations hinder the underlying absorbing signal due to the dissolved organic matter. In this study, TSS absorption at 440 appears to equate the corresponding CDOM absorption for the same wavelength. In addition, CHL absorption at ~ 440 *nm* also affects CDOM absorption signal when CHL concentrations are high.

This argument is further demonstrated with simulations, shown in Figure 4, where the relationships between $a_{CDOM}(440)$ and the response in the CA band for different levels of TSS/CHL concentrations are illustrated. While surface reflectance decreases by increasing CDOM absorption for low levels of TSS/CHL concentrations, variations of CDOM absorption in the medium to high TSS/CHL concentration does not alter surface reflectance. Therefore, with the measured/estimated IOPs for this study, CDOM absorption retrieval in the plume area (case II waters) was not feasible. Nonetheless, variations of dissolved organic matter and its absorbing effects on CA and CA-B ratio bands were detectable when TSS/CHL concentrations remained below 0.5 units in the clear waters (Figure 3). In this figure, the out-of-bound values, indexed five, indicate areas for which high TSS/CHL concentrations were predicted.

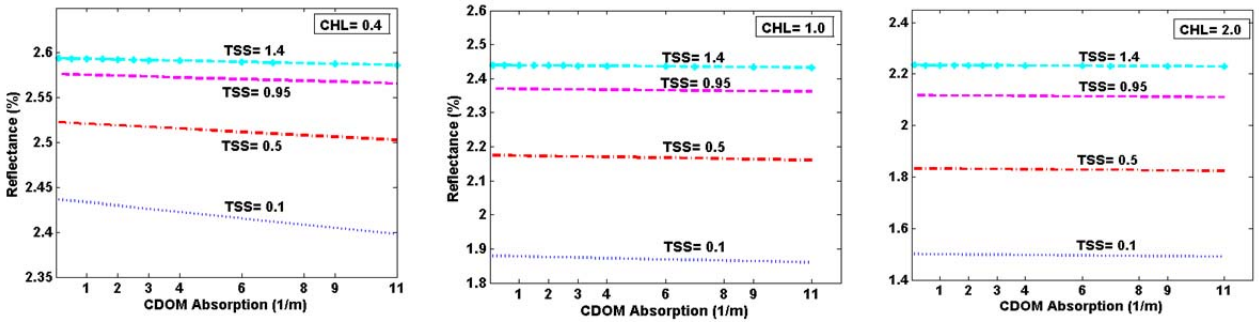

Figure 4. The relationship between CDOM absorption @ 440 *nm* and the SR of the CA band for different levels of TSS/CHL concentrations. Variability of CDOM absorption is detectable using OLI's CA band under low concentrations of TSS/CHL. In turbid waters, CDOM absorption signal is affected by total particle absorption. The values shown on x-axis denote the scaling factors that vary $a_{CDOM}(440)$.

Error maps. The EMAPs were also generated using Eq. 2. The percent difference errors between the two curves indicate how well a modeled curve matches the corresponding image-derived curve.
The disparity between the two curves can imply errors associated with the spatial variability of IOPs, the reliability of the atmospheric correction method, the instruments, and the environmental conditions. Figure 3 demonstrates the resultant error maps associated with the L7 and OLI SR products. The relatively low errors in the plume areas, less than 3% and 5% for OLI and L7, appear to verify the robustness of the atmospheric compensation procedure. In addition, by visually inspecting these maps, one can infer that the error maps are signal-dependent. Low error levels correspond to the turbid waters in which concentrations of TSS /CHL are rather high. In contrast, throughout the clear waters, errors are five times greater, on average, for both sensors. In other words, low levels of signal arising from small patches ($30\times30\ m^2$) of clear waters ($\rho<1\%$) may not be accurately retrieved because of the intervening atmosphere and sensor calibration issues. In such areas, signal arising from the water body is also more susceptible to environmental conditions, such as wind speed and wind direction, causing variable surface facets and complex refraction at the surface. These effects demand well calibrated sensors with spectral bands designed with high SNR for low reflective targets.

Smoothed Water Constituent Maps

Figure 5 shows the associated retrieved constituent maps. Clearly, the averaging method significantly reduced the number of "bad" pixels of L7, shown in Figure 3. As a result, all of the pixels of the two SR products were undergone through the constituent retrieval process. Following the smoothing, the most significant change occurred in the CDOM absorption map where the CDOM absorption values, on average, reduced by 22% resulting in $a_{CDOM}(440)\approx0.12\ m^{-1}$. In other words, averaging removed the unrealistic, high frequency variations in local neighborhoods. Although the average TSS- and CHL-OLI concentrations remained unchanged, the TSS- and CHL-L7 concentrations were boosted by 22% throughout the case II waters leading to $1.85\ gm^{-3}$ and $2.64\ ugl^{-1}$, respectively.

SUMMARY

This paper examined the applicability of the new generation of Landsat sensors (OLI) in water quality studies. With its enhanced features including higher SNR, increased radiometric fidelity, and the addition of a short blue band centered at 440 *nm*, OLI enables obtaining water constituent maps superior to those derived from the existing Landsat (L7). This was demonstrated via a LUT approach where a physics-based model was used to simulate water-leaving reflectances for various combinations of water constituents. The surface reflectance products were compared against those derived from MODIS and simulations. The retrieved chlorophyll maps were validated with a MODIS-derived chlorophyll distribution map and the errors were reported. The concentrations of suspended solids, however, measured in the river/river mouth were utilized to validate the TSS concentration maps. The results showed that OLI is capable of retrieving high-fidelity CHL maps with respect to L7 primarily due to its CA band.

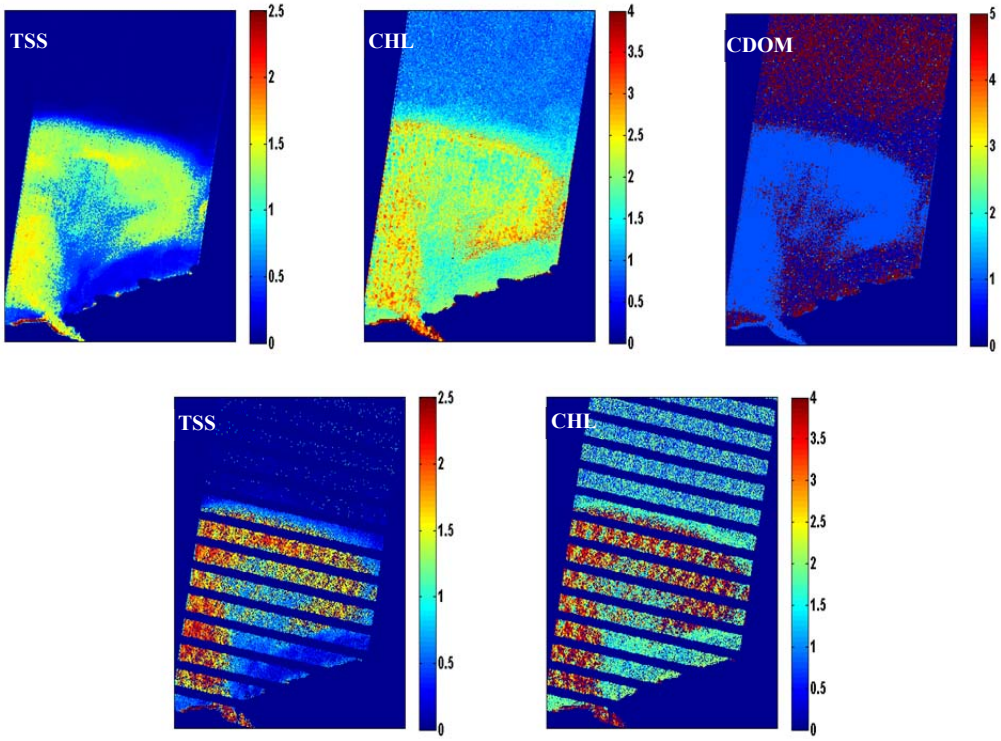

Figure 5. Water constituent maps obtained from the smoothed SR products derived from the simulated OLI (upper row) and L7. The maps from left to right denote TSS, CHL, and CDOM absorption. The low variability of CDOM absorption as well as CHL maps are noticeable.

In addition, as expected, this band allows for mapping CDOM absorption throughout clear waters at low CHL/TSS concentrations. Nevertheless, the TSS maps derived from L7 are reasonably comparable to that of OLI even though L7 tends to overestimate the concentrations. This overestimation is attributed to the calibration issues associated with L7's red band which, along with the green band, exhibits a strong correlation with the TSS concentrations. In addition, the low radiometric fidelity of L7 contributes to the overestimation of the concentrations in the proposed LUT approach. The higher concentration levels are on the order of 10.5% relative to OLI data. In order to more realistically evaluate OLI's potential in such studies, the SR products were smoothed to improve the SNR resembling the desired design specification. The constituent maps derived from the enhanced SNR products appear to remove local variability of the concentration maps, in particular of the CHL maps. The produced error maps assisted in verifying the robustness of the IOPs and the atmospheric compensation technique. The error levels throughout the plume area turn out to be less than 3% and 5% for OLI and L7, respectively.

It should be noted that in this study the differences in the acquisition geometries were not taken into account. It is believed that this difference introduces a negligible error in the constituent retrieval process. The present study will be further extended by examining the retrieved constituent maps against the Hyperion-derived maps as a best-

case scenario achieved by a remote sensing system. The IOPs estimated for the clear waters will be more robustly validated against other research conducted in the western Lake Ontario basin as well.

ACKNOWLEDGMENTS

The authors appreciate the staff at the Research Computing (RC) center of RIT for facilitating the computational burden of this study. We also would like to thank Nina Gibson Raqueno, Rolando Raqueno, Aaron Gerace, and Anthony Vodacek of the Digital Imaging and Remote Sensing Laboratory (DIRS) for their assistance and the previous research efforts in similar studies conducted at RIT. The authors are thankful to Anna C. Tyler of the Biology Department at RIT for granting access to her facilities in Aquatics Laboratory.

APPENDIX A

The following tables contain the correlation coefficients, mean, and coefficient of variations (CV) calculated for the concentration maps. The correlation coefficients, i.e., $-1 < r < +1$, are computed between each constituent map and the individual OLI/L7 bands. The CA-B and B-G bands indicate the band ratios of the CA over the blue and the blue over the green band, respectively. The CVs specify the variability in each band and are calculated as the ratio of the standard deviation and the mean value. The statistics are computed for the original SR products, prior to applying smoothing, over the turbid and clear waters.

Table 3-A. The statistics derived from the TSS- and CHL-L7 products

Water type	Constituent	*Mean*	*CV*	*r*			
				B-G	Blue	Green	Red
Turbid	CHL	2.24	0.42	-0.24	-0.29	0.02	0.44
	TSS	1.6	0.21	-0.35	0.34	0.65	0.73
Clear	CHL	1.4	1.2	-0.16	-0.43	-0.05	-0.01
	TSS	0.07	1.5	-0.13	0.81	0.85	0.45

Table 4-A. The statistics derived from the TSS- and CHL-OLI products

Water type	Constituent	*Mean*	*CV*	*r*					
				CA-B	B-G	CA	Blue	Green	Red
Turbid	CHL	2.15	0.26	-0.64	-0.38	-0.86	-0.38	-0.03	0.00
	TSS	1.3	0.14	-0.49	-0.66	-0.33	0.45	0.89	0.78
Clear	CHL	0.97	1.6	-0.58	-0.34	-0.66	-0.15	0.28	0.07
	TSS	0.03	2.03	0.52	-0.27	0.43	-0.22	0.14	-0.11

REFERENCES

Barsi, J. A. (2011). Personal communications. Greenbelt, MD, USA.

Berk, A., L. Bernstein, et al. (1989). MODTRAN: a moderate resolution model for LOWTRAN 7, Spectral Sciences.

Binding, C. E., D. G. Bowers, et al., (2005). Estimating suspended sediment concentrations from ocean colour measurements in moderately turbid waters; the impact of variable particle scattering properties. *Remote Sensing of Environment* 94(3): 373-383.

Binding, C. E., J. H. Jerome, et al., (2008). Spectral absorption properties of dissolved and particulate matter in Lake Erie. *Remote Sensing of Environment* 112(4): 1702-1711.

Bowers, D. G., K. M. Braithwaite, et al., (2009). Light scattering by particles suspended in the sea: The role of particle size and density. *Continental Shelf Research* 29(14): 1748-1755.

Gerace, A. D. (2010). Demonstrating Landsat's New Potential to Monitor Coastal and Inland Waters. Imaging Science Rochester, Rochester Institute of technology. Ph.D. Thesis**:** 172.

Gordon, H. R., (1978). Removal of atmospheric effects from satellite imagery of the oceans. *Appl. Opt.* 17(10): 1631-1636.

Gordon, H. R., (1990). Radiometric considerations for ocean color remote sensors. *Applied Optics* 29(22): 3228-3236.

Hakvoort, H., J. de Haan, et al., (2002). Towards airborne remote sensing of water quality in The Netherlands--validation and error analysis. *ISPRS Journal of Photogrammetry and Remote Sensing* 57(3): 171-183.

Hayashida, T., J. F. Atkinson, et al., (1999). A Numerical Study of the Niagara River Discharge Near-Shore Flow Field in Lake Ontario. *Journal of Great Lakes Research* 25(4): 897-909.

Jensen, J. R., (2006). *Remote Sensing Of The Environment: An Earth Resource Perspective*,Prentice Hall, Upper Saddle River.

Mobley, C. D., (1994). *Light and Water: Radiative transfer in natural waters*,Academic Press, Inc.

Mobley, C. D., Sundman, L.K. (2008). Hydrolight 5, Ecolight5 User Guide. Bellevue, Sequoia Scientific, Inc.**:** 97.

Raqueno, R. V. (2003). Hyperspectral Analysis Tools for Multiparameter Inversion of Water Quality Factors in the Lake Ontario Rochester Embayment. Environmental and Resource Engineering. Syracuse, State University of New York. Ph.D. Thesis**:** 165.

Sanders, L. C., J. R. Schott, et al., (2001). A VNIR/SWIR atmospheric correction algorithm for hyperspectral imagery with adjacency effect. *Remote Sensing of Environment* 78(3): 252-263.

Schott, J. R., (2007). *Remote Sensing The Image Chain Approach*,Oxford Unversity Press, New York.

Schowengerdt, R. A., (2007). *Remote Sensing: Models and Methods for Image Processing*,Elsevier, Burlington, MA.

Thiemann, S. and H. Kaufmann, (2002). Lake water quality monitoring using hyperspectral airborne data--a semiempirical multisensor and multitemporal approach for the Mecklenburg Lake District, Germany. *Remote Sensing of Environment* 81(2-3): 228-237.